# Graph-based Spatial-temporal Feature Learning for Neuromorphic Vision Sensing

Yin Bi, Aaron Chadha, Alhabib Abbas, Eirina Bourtsoulatze and Yiannis Andreopoulos
Department of Electronic & Electrical Engineering
University College London, London, U.K.
{yin.bi.16, aaron.chadha.14, alhabib.abbas.13, e.bourtsoulatze, i.andreopoulos}@ucl.ac.uk

## Abstract

*Neuromorphic vision sensing (NVS) devices represent visual information as sequences of asynchronous discrete events (a.k.a., "spikes") in response to changes in scene reflectance. Unlike conventional active pixel sensing (APS), NVS allows for significantly higher event sampling rates at substantially increased energy efficiency and robustness to illumination changes. However, feature representation for NVS is far behind the APS-based counterparts, resulting in lower performance in high-level computer vision tasks. To fully utilize the sparse and asynchronous nature, we propose a compact graph representation for NVS, which allows for end-to-end learning with graph convolution neural networks. We couple this with a novel end-to-end feature learning framework that accommodates both appearance-based and motion-based tasks. The framework is comprised of a spatial feature learning module, which utilizes our proposed residual-graph CNN (RG-CNN), for end-to-end learning of appearance-based features directly from graphs. We extend this with our proposed Graph2Grid block and temporal feature learning module for efficiently modelling temporal dependencies over multiple graphs and a long temporal extent. We show that performance of this framework generalizes to both object classification and action recognition, importantly preserving the spatial and temporal coherence of spike events, while requiring less computation and memory. We show that our proposed framework outperforms all recent methods on standard datasets. Finally, to address the absence of large real-world NVS datasets for complex recognition tasks, we introduce, evaluate and make available a 100k dataset of NVS recordings of the American Sign Language letters (ASL_DVS) acquired with an iniLabs DAVIS240c device under real-world conditions, as well as a neuromorphic action recognition dataset (UCF101_DVS and HMDB51_DVS) recorded from monitor.*

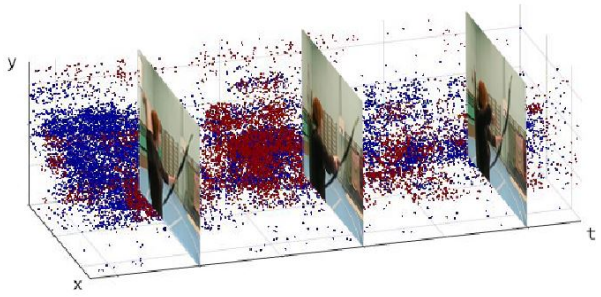


Figure 1: Examples of archery action captured by APS and NVS sensors. APS sensors capture images at fixed frame rates, while NVS sensors output a stream of events. (Red:ON, Blue:OFF)

## 1. Introduction

With the prevalence and advances of CMOS active pixel sensing (APS) and deep learning, researchers have achieved good performance in APS-based computer vision tasks, such as object detection [30, 68, 45], object recognition [36, 23] and action recognition[84, 73, 80, 15]. However, APS cameras suffer from the following problems: limited frame rate, high redundancy between frames, blurriness due to slow shutter adjustment under varying illumination, and high power requirements [21] which thus limits the effectiveness of APS-based frameworks. To solve these problems, researchers have devised neuromorphic vision sensing (NVS) sensors such as the iniLabs DAVIS cameras [22] and the Pixium Vision ATIS cameras [62], which are inspired by the photoreceptor-bipolar-ganglion cell information flow in mammalian vision. NVS sensors generate output (i.e., spikes) asynchronously only when the transient change of illumination intensity exceeds a certain threshold in a scene, instead of recording entire frames at fixed frame rates, independent of any activity in the scene (as per APS sensors). The output of the NVS sensor is represented asynchronously as a collection of tuple sequences, referred to as an Address Event Representation (AER)[6], which contains the spatio-temporal coordinates of the re-

flectance events along with the event polarity (i.e., ON or OFF). The event polarity indicates an increase (ON) or decrease (OFF) in illumination intensity. As an illustration, Fig. 1 shows a neuromorphic event stream, overlaid with the corresponding RGB frames recorded at the video framerate; events are plotted according to their spatio-temporal coordinates and color coded as blue (OFF) and red (ON). Notably, there are many more intermediate events between the RGB frames, which indicates the substantially higher framerate achievable with an NVS sensor and asynchronous outputs. Furthermore, the asynchronicity removes the data redundancy from the scene, which reduces to the power requirement to 10mW, compared to 14W for APS sensors. Remarkably, NVS sensors achieve this with microsecond-level latency and robustness to uncontrolled lighting conditions as no synchronous global shutter is used.

Beyond event sparsity and asynchronicity, neuromorphic event streams are naturally encoding spatio-temporal motion information [21]; as such, they are extremely adaptable to tasks related to moving objects such as action analysis/recognition, object tracking or high-speed moving scenes. We therefore look to perform feature learning directly on the raw neuromorphic events. This is in contrast to recent work on action analysis/recognition [26], which relies on extracting spatio-temporal features from RGB frames and thus inherits the limitations associated with APS cameras.

Unfortunately, effective methods for representation learning on neuromorphic events to solve complex computer vision tasks are currently limited and outperformed by their APS-based counterparts. This is partly due to a limited research in the NVS domain, as well as a lack of NVS data with reliable annotations to train and test on [21, 52, 79]. Yet, more so, the sheer abundance of asynchronous and sparse events means that feature learning directly on events can be particularly cumbersome and unwieldy. Thus far, most approaches have attempted to solve this issue by either artificially grouping events into frame forms [88, 19, 14, 13] or deriving complex feature descriptors [75, 18, 39], which do not always provide for good representations for complex tasks like object classification. Moreover, such approaches dilute the advantages of the asynchronicity of NVS streams by limiting the frame-rate, and may be sensitive to the noise and change of camera motion or viewpoint orientation. Finally these methods fail to model long temporal event dependencies explicitly, thus rendering them less viable for action recognition and action similarity-based tasks. More recent methods have employed end-to-end feature learning, where a convolutional neural network (CNN) [29, 2] or spiking neural network (SNN) [8, 24] is trained to learn directly from raw observations. While these methods show great promise, CNN-based learning methods require event grouping into frames and therefore suffer from the same drawbacks as above. On the other hand, SNN-based methods are complex to train, which results in lower performance compared to gradient-based alternatives.

In this work, we propose an end-to-end feature learning framework trained directly on neuromorphic events. However, instead of using CNNs or SNNs, we propose to leverage on graph-based learning. By represent events as graphs, we are able to maintain event asynchronocity and sparsity, while performing training with traditional gradient-based backpropagation. To the best of our knowledge, this is the first attempt to represent neuromorphic spike events as graphs, and the first time neuromorphic events have been trained with graph convolution neural networks and end-to-end feature learning.

Our proposed graph based framework is able to accommodate both appearance and motion-based tasks; in this paper, we focus on object classification and action recognition as representative tasks. For object classification, we design a spatial feature learning module, comprising graph convolutional layers and graph pooling layers, for processing a single input event graph. For action recognition, we extend this module with temporal feature learning, in order to learn a spatio-temporal representation over the entire input. Specifically, we introduce a Graph2Grid block for aggregating a sequence of graphs over a long temporal extent. Each event graph in the sequence is first processed by a spatial feature learning module; the mapped graphs are then converted to grid representation by the Graph2Grid block and the resulting frames are stacked, for processing with any conventional 2D or 3D CNN. This is inspired by recent work in APS-based action recognition [26] that processes multiple RGB frames with 2D CNNs and aggregates the learned representations with a 3D convolution fusion and pooling.

In order to address the lack of NVS data for evaluation, we introduce the largest sourced NVS dataset for object classification, which we refer to as ASL-DVS. The task is to classify the hand recordings as one of 24 letters from the American Sign Language (ASL). For action recognition, we leverage on existing APS-based datasets such as UCF-101 and HMDB-51, and convert these to the NVS domain by recording the display with an NVS camera. The generated NVS datasets, UCF101_DVS and HMDB51_DVS, represent the largest NVS datasets for action recognition. We evaluate our framework on both object classification and action recognition in Sec. 4 and show that our framework achieves state-of-the-art results on both tasks compared to recent work or conventional frame-based approaches.

We summarize our contributions as follows:

1. We propose a graph based representation for neuromorphic events, allowing for fast end-to-end graph based training and inference.

2. We design a new graph-based spatial feature learning module, We evaluate performance of this module on object classification.

3. We extend our spatial feature learning module with our Graph2Grid block and temporal feature learning module for efficiently modelling coarse temporal dependencies over multiple graphs. We evaluate performance of the end-to-end learning framework on action recognition.

4. We address the lack of NVS data for training and inference by introducing new datasets for NVS-based object classification (ASL-DVS) and action recognition (UCF101_DVS and HMDB51_DVS), and make these available to the research community.

In Section 2 we review related work. Section 3 details our method for graph-based spatio-temporal feature learning network for activity recognition. Two downstream applications are presented in Section 4 and Section 5 concludes the paper.

## 2. Related Work

There are mainly two types of feature representation; handcrafted feature extraction and end-to-end trainable feature learning in neuromorphic vision sensing area. We will describe these two types in the following section.

Handcrafted feature descriptors are widely used by neuromorphic vision community. Some of the most common descriptors are corner detectors and line/edge extraction [17, 82, 49, 50]. While these efforts were promising early attempts for NVS-based object classification, their performance does not scale well when considering complex datasets. Inspired by their frame-based counterparts, optical flow methods have been proposed as feature descriptors for NVS [18, 5, 3, 4, 11, 55]. For a high-accuracy optical flow, these methods have very high computational requirements, which diminishes their usability in real-time applications. In addition, due to the inherent discontinuity and irregular sampling of NVS data, deriving compact optical flow representations with enough descriptive power for accurate classification and tracking still remains a challenge [18, 5, 11, 55]. Later, Orchard *et al.* introduced HFirst descriptors that used spike timing to encode the strength of events and implemented a max operation to output a number representing the strength input [57]. Lagorce *et al.* proposed event based spatio-temporal features called time-surfaces [38]. This is a time oriented approach to extract spatio-temporal features that are dependent on the direction and speed of motion of the objects. Inspired by time-surfaces, Sironi proposed a higher-order representation for local memory time surfaces that emphasizes the importance of using the information carried by past events to obtain a robust representation [75]. Recently Ramesh *et al.* introduced a generic visual descriptor termed as DART that encodes the structural context using log-polar grids for events [67]. These descriptors is much sensitive to noise and strongly depend on the type of object motion in scene. Moreover, these descriptors have only proven to be useful for static object recognition, and they fail to take temporal information into account and maintain a representation of dynamics over a long time so that they may not be useful for long-term application such as action recognition evaluated in this work.

Two end-to-end feature learning methods are proposed. The first type is frame-based methods: the main idea is to construct events to grid frame form, then apply covolution neural networks for the feature learning. i.e., converting the neuromorphic events to into synchronous frames of spike events, on which conventional computer vision techniques can be applied. Zhu *et al.* [88] introduced a four-channel image form with the same resolution as the neuromorphic vision sensor: the first two channels encode the number of positive and negative events that have occurred at each pixel, while last two channels as the timestamp of the most recent positive and negative event. Inspired by the functioning of Spiking Neural Networks (SNNs) to maintain memory of past events, leaky frame intergration has been used in recent work [19, 14, 13], where the corresponding position of the frame is incremented of a fixed amount when a event occurs at that event address. Peng *et al.* [59] proposed bag-of-events (BOE) feature descriptors, which is a statistical learning method that firstly divides the event streams into multiple segments and then relies on joint probability distribution of the consecutive events to represent feature maps. Amir *et al.* used temporal filter to process the events, regarded the filter cascades as stacking frames and input these frames to Convolution Neural Networks [2]. Similary, Ghosh *et al.* partitioned events into a three dimensional grid of voxels where spatio-temporal filters are used to learn the feature, and learnt feature are as input to feed to convolution neural networks for action recognition [29]. Chadha *et al.* [16] generated frames by summing the polarity of events in each address as pixel, then fed them into a multi-modal teacher-student framework, where it employs a pre-trained optical flow stream as a teacher network to transfer knowledge to the NVS student network . While useful for early-stage attempts, all of these methods are frame-based methods that are not suitable for the neuromorphic event's sparse and asynchronous nature since the frame sizes that need to be processed are substantially larger than those of the original NVS streams. The advantages of event-based sensors are diluted if their event streams are cast back into synchronous frames for the benefit of conventional processors downstream, thus not providing an efficient and power-saving learning systems.

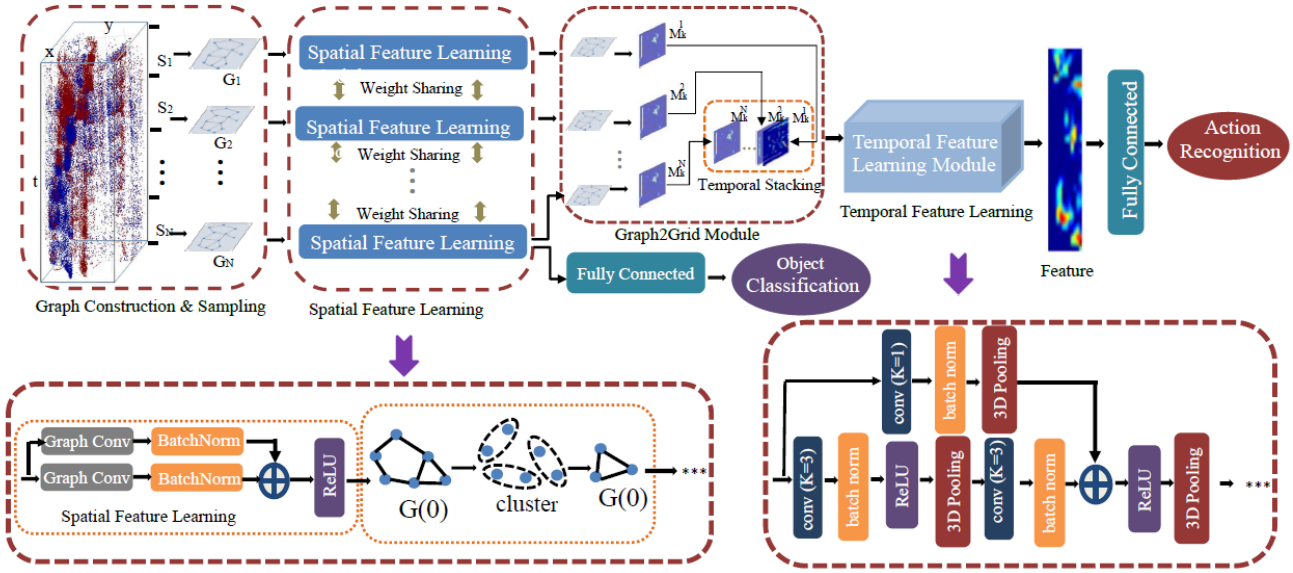


Figure 2: Framework of graph-based action recognition for neuromorphic vision sensing. Our framework is able to accommodate both object classification and action recognition tasks. We first construct $S$ graphs from the event stream (where $S = 1$ for object classification), and each graph is passed through a spatial feature learning module, comprising graph convolutional and pooling layers. For object classification, the output of this module is mapped to object classes directly by fully connected layers. For action recognition, we model coarse temporal dependencies over multiple graphs by converting to a grid representation via the Graph2Grid module and perform temporal feature learning with a conventional 3D CNN, before mapping features to action classes with fully connected layers.

The second type of end-to-end feature learning method is event-based methods. The most commonly used architecture is based on spiking neural networks (SNNs) [1, 24, 8, 40, 51]. While SNNs are theoretically capable of learning complex representations, they have still not achieved the performance of gradient-based methods because of lack of suitable training algorithms. Essentially, since the activation functions of spiking neurons are not differentiable, SNNs are not able to leverage on popular training methods such as backpropagation. To address this, researchers currently follow an intermediate step [54, 25, 60, 77]: a neural network is trained off-line using continuous/rate-based neuronal models with state-of-the-art supervised training algorithms and then the trained architecture is mapped to an SNN. However, until now, despite their substantial implementation advantages at inference, the obtained solutions are complex to train and have typically achieved lower performance than gradient-based CNNs. There is some other initial attempts on event-based feature learning for neuromorphic vision sensing. Besides using SNNs, Wang interpreted an event sequence as a 3D point clouds in space and time, event cloud is hierarchically fed in PointNet[64] to capture spatio-temproal structure of motion, then the learned feature is used for recognition[85]. While useful for early-stage attempts, all of these methods were test on simple datasets with a small number of class and clean background: DVS128 Gesture Dataset used in [2, 85] comprises a set of 11 hand and arm gestures and posture dataset in [87, 58] includes only three human actions, i.e., bend, sitsand, and walk. Moreover, used datasets all were acquired from the experimental environment that cannot represent complex real-life scenarios, so that initial algorithms achieved high performance on these datasets. Moreover, there is doubt that these methods can be apply for the complex dataset from real-life scenarios since they cannot capture long term dependencies across time. When these work on complex dataset (such as UCF101_DVS) for human action recognition, their performance degrades significantly as discussed in application experiments.

## 3. Methodology

The architecture for our graph-based spatio-temporal feature learning network is shown in the Fig. 2, and is comprised of four parts: graph construction and sampling, spatial feature learning module, Graph2Grid module and temporal feature learning module. The neuromorphic events are firstly sampled and connected with a sequence of graphs. For object classification, a single graph is typically constructed, whereas for action recognition with longer temporal extent, multiple graphs are extracted over the event stream duration. The graph(s) are then individually processed by a spatial feature learning module, which consists of multiple graph convolution and pooling layers to map the

input to a coarser graph encoding. For object classification and other appearance-based applications, we obtain a single graph encoding that we pass to a single fully connected layer for prediction. Conversely, for action recognition, we obtain multiple graph encodings. As such, we convert the graphs to a grid representation with our Graph2Grid module and stack the resulting frames, for temporal feature learning with a 3D CNN. In this way, we are able to effectively and efficiently learn spatio-temporal features for motion-based applications, such as action recognition. We provide more details on each component of the framework in the following sections.

### 3.1. Graph Construction

Given a NVS sensor with spatial address resolution of $H \times W$, we express a volume of events $V$ produced by an NVS camera as a tuple sequence:

$$\{e_i\}_N = \{x_i, y_i, t_i, p_i\}_N \tag{1}$$

where $(x_i, y_i) \in [1, H] \times [1, W]$ indicates the spatial address at which the spike event occurred, $t_i$ is the timestamp indicating when the event was generated, $p_i \in \{+1, -1\}$ is the event event polarity (with +1, -1 signifying ON and OFF events respectively), and $N$ is the total number of the events.

To reduce the storage and computational cost, we use non-uniform grid sampling [41] to sample a subset of $M$ representative events $\{e_i\}_M \subset \{e_i\}_N$, where $M \ll N$. Effectively, one event is randomly selected from a space-time volume with the maximum number of events inside. If we consider $\mathbf{s}\{e_i\}_{i=1}^{k}$ to be such a grid containing $k$ events, then only one event $e_i$ ($i \in [1, k]$) is randomly sampled in this space-time volume. We then define the sampling events $\{e_i\}_{\{M\}}$ on a directed graph $\mathrm{G} = \{\nu, \varepsilon, \mathrm{U}\}$, with $\nu$ being the set of vertices, $\varepsilon$ the set of the edges, and U the coordinates of the nodes that locally define the spatial relations of the nodes. The sampling events are independent and not linked, therefore, we regard each event $e_i : (x_i, y_i, t_i, p_i)$ as a node in the graph, such as that $\nu_i : (x_i, y_i, t_i)$, with $\nu_i \in \nu$. We define the connectivity of nodes in the graph based on the radius-neighborhood-graph strategy. Namely, neighboring nodes $\nu_i$ and $\nu_j$ are connected with an edge only if their weighted Euclidean distance $d_{i,j}$ is less than radius distance R. For two spike events $e_i$ and $e_j$, the Euclidean distance between them is defined as the weighted spatio-temporal distance:

$$d_{i,j} = \sqrt{\alpha(|x_i - x_j|^2 + |y_i - y_j|^2) + \beta|t_i - t_j|^2} \leq \mathrm{R} \tag{2}$$

where $\alpha$ and $\beta$ are weight parameters compensating for the difference in spatial and temporal grid resolution (timing accuracy is significantly higher in NVS cameras than spatial grid resolution). To limit the size of the graph, we constrain the maximum connectivity degree for each node by parameter $D_{\max}$. We subsequently define $u(i, j)$ for node $i$, with connected node $j$, as $u(i, j) = [|x_i - x_j|, |y_i - y_j|] \in \mathrm{U}$.

After connecting all nodes of the graph $\mathrm{G} = \{\nu, \varepsilon, \mathrm{U}\}$ via the above process, we consider the polarity of events as a signal that resides on the nodes of the graph G. In other words, we define the input feature for each node $i$, as $f^{(0)}(i) = p_i \in \{+1, -1\}$.

We introduce the parameter $S$ to represent the number of graphs constructed from one sample. Given that object classification is appearance-based and typically only requires a short temporal extent, therefore we set $S = 1$. Specifically, we randomly extract $T_V$ length events over the entire event stream to construct a graph. Conversely, for action recognition, we divide the event stream into $S$ volumes with the same time duration, then we construct a graph for each volume in which $T_V$ ($T_V < T/S$, where $T$ is sample duration) length events are randomly extracted to construct a graph, giving us a set of graphs $\mathcal{G} = \{\mathrm{G}_n\}_{n=1}^{S}$. In this way, we efficiently model coarse temporal dependencies over the duration of the video, without constructing a single large and substantially complex graph. The graphs can thus be processed individually by our spatial feature learning module before fusion with our Graph2Grid module and temporal feature learning. This is inspired by recent work on action recognition with RGB frames [26], which fuses representations over coarse temporal scales with 3D convolutions and pooling; indeed, our graph-based framework is substantially more lightweight and does not suffer from the limitations of active pixel sensing.

### 3.2. Spatial Feature Learning Module

The constructed graphs are first fed individually into a spatial feature learning module, where our framework learns appearance information. According to the common architectural pattern for feed-forward neural networks, these graph convolutional neural networks are built by interlacing graph convolution layer and graph pooling layers, where the graph convolution layer performs a non-linear mapping and the pooling layer reduces the size of the graph.

Graph convolution generalizes the traditional convolutional operator to the graph domain. Similar to frame-based convolution, graph convolution can be categorized into two types [10]: spectral and spatial. Spectral convolution [20, 83, 12, 70, 72] defines the convolution operator by decomposing a graph in the spectral domain and then applying a spectral filter on the spectral components. However, this operation requires identical graph input and handles the whole graph simultaneously, so it is not suitable for the variable and large graphs constructed from NVS. On the other hand, spatial convolution [9, 27, 46, 48] aggregates a new feature vector for each vertex, using its neighborhood information weighted by a trainable kernel function. Because of

this property, we consider spatial convolution operation as a better choice when dealing with graphs from NVS.

Similar to conventional frame-based convolution, spatial convolution operations on graphs are also a one-to-one mapping between kernel function and neighbors at relative positions w.r.t. the central node of the convolution. Let $i$ denote a node of the graph with feature $f(i)$, $\mathcal{N}(i)$ denote the set of neighbors of node $i$ and $g(u(i,j))$ denote the weight parameter constructed from the kernel function $g(.)$. The graph convolution operator $\otimes$ for this node can then be written in the following general form:

$$(f \otimes g)(i) = \frac{1}{|\mathcal{N}(i)|} \sum_{j \in \mathcal{N}(i)} f(j) \cdot g(u(i,j)) \qquad (3)$$

where $|\mathcal{N}(i)|$ is the cardinality of $\mathcal{N}(i)$. We can generalize (3) to multiple input features per node. Given the kernel function $\mathbf{g} = (g_1, ..., g_l, ..., g_{M_{in}})$ and input node feature vector $\mathbf{f}_l$, with $M_{in}$ feature maps indexed by $l$, the spatial convolution operation $\otimes$ for the node $i$ with $M_{in}$ feature maps is defined as:

$$(\mathbf{f} \otimes \mathbf{g})(i) = \frac{1}{|\mathfrak{N}(i)|} \sum_{l=1}^{M_{in}} \sum_{j \in \mathfrak{N}(i)} f_l(j) \cdot g_l(u(i,j)) \qquad (4)$$

The kernel function $\mathbf{g}$ defines how to model the coordinates U. The content of U is used to determine how the features are aggregated and the content of $f_l(j)$ defines what is aggregated. As such, several spatial convolution operations [9, 27, 46, 48] on graphs were proposed by using different choice of kernel functions. Among them, SplineCNN [27] achieves state-of-the-art results in several applications, so in our work we use the same kernel function as in SplineCNN. In this way, we leverage properties of B-spline bases to efficiently filter NVS graph inputs of arbitrary dimensionality. Let $((N^m_{1,i})_{1 \le i \le k_1}, ..., (N^m_{d,i})_{1 \le i \le k_d})$ denote $d$ open B-spline bases of degree $m$ with $\mathbf{k} = (k_1, ..., k_d)$ defining $d$-dimensional kernel size [61]. Let $w_{\boldsymbol{z},l} \in \mathbf{W}$ denote a trainable parameter for each element $\boldsymbol{z}$ from the Cartesian product $\mathcal{Z} = (N^m_{1,i})_i \times \cdots \times (N^m_{d,i})_i$ of the B-spline bases and each of the $M_{in}$ input feature maps indexed by $l$. Then the kernel function $g_l : [a_1, b_1] \times \cdots \times [a_d, b_d] \to \mathbb{R}$ is defined as

$$g_l(\mathbf{u}) = \sum_{\boldsymbol{z} \in \mathcal{Z}} w_{\boldsymbol{z},l} \cdot \prod_{i=1}^{d} N_{i,z_i}(u_i) \qquad (5)$$

We denote a graph convolution layer as $\mathrm{Conv}(M_{\mathrm{in}}, M_{\mathrm{out}})$, where $M_{\mathrm{in}}$ is the number of input feature maps and $M_{\mathrm{out}}$ is the number of output feature maps indexed by $l^{'}$. Then, a graph convolution layer with bias $b_l$, activated by activation function $\xi(t)$, can be written as:

$$\begin{aligned} \mathrm{Conv}_{l'} \quad = \quad & \xi\Big(\frac{1}{|\mathcal{N}(i)|} \sum_{l=1}^{M_{\mathrm{in}}} \sum_{j \in \mathfrak{N}(i)} f_l(j) \cdot \sum_{\boldsymbol{z} \in \mathcal{Z}} w_{z,l} \qquad (6) \\ & \cdot \quad \prod_{i=1}^{d} N_{i,z_i}(u_i) + b_{l'}\Big) \end{aligned}$$

where $l^{'} = 1, .., M_{\mathrm{out}}$, indicates the $l^{'}$th output feature map. This defines a single graph convolutional layer. For $C$ consecutive graph convolutional layers, $(\mathrm{Conv}^{(c)})_{c \in [0,C]}$, the $c$-th layer has corresponding input feature map $\mathbf{f}^{(c)}$ over all nodes, with the input feature for node $i$ of the first layer $\mathrm{Conv}^{(0)}$, $f^{(0)}(i) = p_i \in \{+1, -1\}$.

To accelerate deep network training, we use batch normalization [34] before the activation function. That is, the whole node feature $f_{l'}$ over the $l^{'}$-th channel map is normalized individually via

$$f^{'}_{l'} = \frac{f_l - E(f_{l'})}{\sqrt{\mathrm{Var}(f_{l'}) + \epsilon}} \cdot \gamma + \beta \quad l^{'} = 1, .., M_{\mathrm{out}} \qquad (7)$$

where $E(f_{l'})$ and $\mathrm{Var}(f_{l'})$ denote mean and variance of $f_{l'}$ respectively, $\epsilon$ is used to ensure normalization does not overflow when the variance is near zero, and $\gamma$ and $\beta$ represent trainable parameters.

**Residual Graph CNNs**: Inspired by the ResNet architecture [32], we propose residual graph CNNs for our spatial feature learning module, in order to resolve the well-known degradation problem inherent with increasing number of layers (depth) in graph CNNs [43]. Our residual graph CNN (RG-CNN) is effectively composed of a series of residual blocks and pooling layers. We note that equations (6) and (7) denote a single graph convolutional layer with batch normalization [34] that accelerates the convergence of the learning process; we apply residual connections in spatial feature learning module by summing element-wise the outputs of graph convolutions. Our "shortcut" connection is comprised of a graph convolution layer with kernel size $K = 1$ for mapping the feature dimension to the correct size, and is also followed by batch normalization. A residual block is illustrated in Fig. 2. We denote the resulting graph residual block as $\mathrm{Res_g}(\mathrm{c_{in}}, \mathrm{c_{out}})$, with $c_{\mathrm{in}}$ input feature maps and $c_{\mathrm{out}}$ output feature maps.

A residual block is followed by max pooling over clusters of nodes; given a graph representation, let us denote the spatial coordinates for node $i$ as $(x'_i, y'_i) \in \mathbb{R}^{H' \times W'}$ and resolution as $H' \times W'$. We define the cluster size as $s_h \times s_w$, which corresponds to the downscaling factor in the pooling layer of $\left\lceil \frac{H'}{s_h} \right\rceil \times \left\lceil \frac{W'}{s_w} \right\rceil$. For each cluster, we generate a single node, with feature set to the maximum over node features $\mathbf{f}$ in the cluster, and coordinates set to the average of node coordinates $(x'_i, y'_i)$ in the cluster. Importantly, if

there are connected nodes between two clusters, we assume the new generated nodes in these two clusters are connected with an edge.

For object classification, where the entire event stream can be modelled by a single graph, we can directly map the output of the spatial feature learning module to the classes with a fully connected layer. Given $M_{\text{in}}$ feature maps $\mathbf{f} \longrightarrow \mathbb{R}^{I \times M_{\text{in}}}$ from a graph with $I$ nodes, similar to CNNs, a fully connected layer in a graph convolutional network is a linear combination of weights linking all input features to outputs. Let us denote $f_l^{\text{spatial}}(i)$ as the $l$th output feature map of the $i$th node of the of the spatial feature learning module, then we can derive a fully connected layer in the graph as:

$$f_q^{\text{FC}}(i) = \xi(\sum_{i=1}^{I}\sum_{l=1}^{M_{\text{in}}} F_{I \times M_{in} \times Q} f_l^{\text{spatial}}(i)) \quad q = 1, ..., Q \tag{8}$$

where $Q$ is the number output channels indexed by $q$, $F$ is trainable weight with $I \times M_{\text{in}} \times Q$ size, $\xi(t)$ is the non-linear activation function, e.g. ReLU: $\xi(t) = \max(0, t)$. For the remainder of the paper, we use $\text{FC}(Q)$ to indicate a fully connected layer with $Q$ output dimensions, comprising the results of (8).

### 3.3. Graph2Grid: from graphs to grid snippet

For action recognition, we need to model temporal dependencies over the entire event stream. As discussed in Section 3.1, given a long video duration, it is not feasible to construct a single graph over the entire event stream, due to the sheer number of events. It is more computationally feasible to generate multiple graphs for time blocks of duration $T_V$. These are processed individually by the spatial feature learning module. However, to model coarse temporal dependencies over multiple graphs, we must fuse the spatial feature representations. We propose a new Graph2Grid module that transforms the learned graphs from our spatial feature learning module to a grid representation and performs stacking over temporal dimension, as illustrated in Fig. 2. In this way. we are effectively able to create pseudo frames from the graphs, with $M_{in}$ channels and timestamp $(n-1)T_V$, corresponding with the $n$-th graph.

Again, denoting the output spatial feature learning map as $f_l^{\text{spatial}}(i)$ for the $l$th output feature map of the $i$th node with coordinates $(x_i', y_i') \in \mathbb{R}^{H_{\text{spatial}} \times W_{\text{spatial}}}$, we define a grid representation $\mathbf{f}^{\text{grid}}(i)$ of spatial size $H_{\text{spatial}} \times W_{\text{spatial}}$ as follows:

$$f_{a,b,l}^{\text{grid}} = \begin{cases} f_l^{\text{spatial}}(i), & \text{when } a = x_i', b = y_i' \\ 0, & \text{otherwise} \end{cases} \tag{9}$$

where $(a, b) \in \mathbb{R}^{H_{\text{spatial}} \times W_{\text{spatial}}}$. The resulting grid feature representation $\mathbf{f}^{\text{grid}} \in \mathbb{R}^{H_{\text{spatial}} \times W_{\text{spatial}} \times M_{in}}$ is for a single graph; for $S$ graphs over the temporal sequence, we simple concatenate over a fourth temporal dimension. We denote the resulting grid feature over $S$ graphs as $\mathbf{F}^{\text{grid}} = \mathbf{f}^{\text{grid},1} || \mathbf{f}^{\text{grid},2} || \ldots || \mathbf{f}^{\text{grid},S}$, where $||$ denotes concatenation over the temporal axis. The dimensions of $\mathbf{F}^{\text{grid}}$ is thus $H_{\text{spatial}} \times W_{\text{spatial}} \times M_{\text{in}} \times S$. This grid feature matrix can thus be fed to a conventional 3D convolutional neural network in our temporal feature learning module, in order to learn coarse temporal dependencies and a full spatio-temporal representation of the input.

### 3.4. Temporal Feature Learning Module

The output feature matrix $\mathbf{F}^{\text{grid}}$ contains both spatial and temporal information over the entire video duration, which can be effectively encoded with a conventional 3D CNN [80] in order to generate a final spatio-temporal representation of the video input for action recognition. In this paper, we consider three network architectures for the 3D CNN; a plain architecture with interlaced 3D convolutional and pooling layers, an I3D-based architecture comprising multiple I3D blocks as configured in [15], and a 3D residual block design. Our 3D residual block design is illustrated in Fig. 2; essentially for $C$ consecutive convolutional layers, every $c-2$-th layer is connected to the $c$-th layer via a non-linear residual connection, for all $c \in \{3, 5 \ldots C-2, C\}$, and every layer is followed by batch normalization. For all architectures, we aggregate the features in the final layer of the CNN with global average pooling and pass to a fully connected layer for classification. We provide further experimental details in Section 4, describing number of input and output channels per layer.

It is worth noting that while 3D CNNs are notorious for being computationally heavy, the NVS camera DAVIS240c has a grid resolution at most equal to $240 \times 180$ and we use graph pooling in our spatial feature learning module, which means the spatial size of $\mathbf{F}^{\text{grid}}$ is at most $30 \times 30$. This is substantially lower input resolution than APS-based counterparts ingesting RGB frames, where the spatial resolution to the 3D CNN is typically $224 \times 224$ or higher.

## 4. Experimental Details and Evaluation

In this section, we demonstrate the potential of our framework as a method of representation learning with NVS inputs, for high-level computer vision tasks. We firstly focus on object classification, as an appearance-based application, in Section 4.1, and then large-scale multi-class human action recognition, as a motion-based application, in Section 4.2. Beyond evaluation on standard datasets, we introduce our newly proposed ASL_DVS dataset in Section 4.1, which is the largest-source dataset for object classification. We additionally generate the largest NVS-based action recognition dataset by converting standard APS datasets,

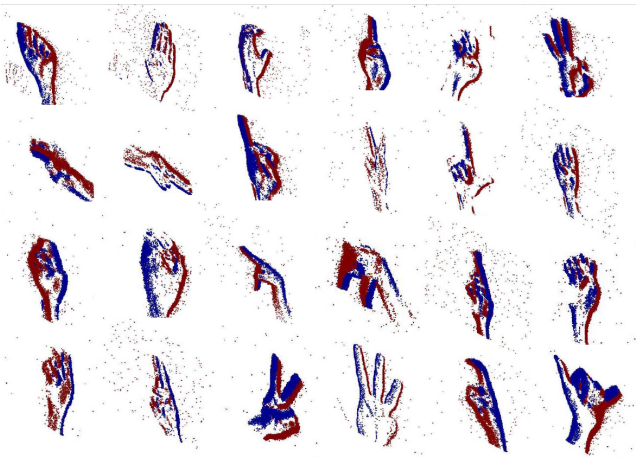

Figure 3: Examples of the ASL-DVS dataset (the visualizations correspond to letters A-Y, excluding J, since letters J and Z involve motion rather than static shape). Events are grouped to image form for visualization (Red/Blue: ON/OFF events).

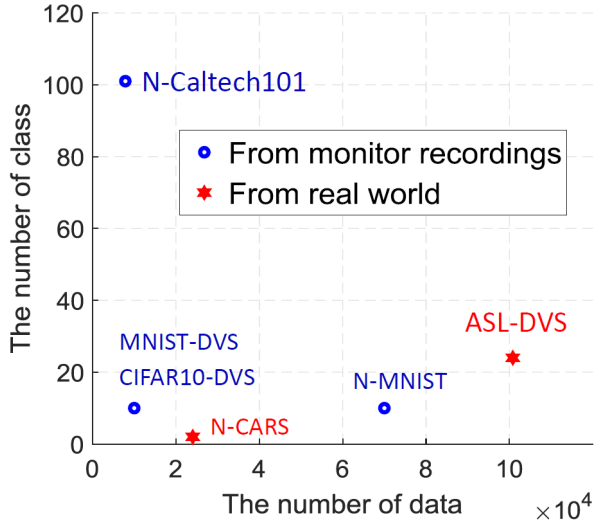


Figure 4: Comparison of proposed NVS dataset w.r.t. the number of class and the number of total size.

UCF-101 and HMDB-51, to the NVS domain and explain the recording process prior to evaluation in Section 4.2.

### 4.1. Object Classification

Object classification finds numerous applications in visual surveillance, human-machine interfaces, image retrieval and visual content analysis systems. We first introduce the datasets we evaluate on, including our new ASL-DVS dataset, before discussing implementation details and presenting results. We compare with recent state-of-the-art methods and performing complexity analysis.

**Datasets:** Many neuromorphic datasets for object classification are converted from standard frame-based datasets, such as N-MNIST [56], N-Caltech101 [56], MNIST-DVS [71] and CIFAR10-DVS [42]. N-MNIST and N-Caltech101 were acquired by an ATIS sensor [63] moving in front of an LCD monitor while the monitor is displaying each sample image. Similarly, MNIST-DVS and CIFAR10-DVS datasets were created by displaying a moving image on a monitor and recording with a fixed DAVIS sensor [44]. Emulator software has also been proposed in order to generate neuromorphic events from pixel-domain video formats using the change of pixel intensities of successively rendered images [50, 7, 28]. While useful for early-stage evaluation, these datasets cannot capture the real dynamics of an NVS device due to the limited frame rate of the utilized content, as well as the limitations and artificial noise imposed by the recording or emulation environment. To overcome these limitations, N-CARS dataset [75] was created by directly recording objects in urban environments with an ATIS sensor. This two-class real-world dataset comprises 12,336 car samples and 11,693 non-car samples (background) with 0.1 second length. Despite its size, given that it only corresponds to a binary classifier problem, N-CARS cannot represent the behaviour of object classification algorithms on more complex NVS-based tasks.

We present a large 24-class dataset of handshape recordings under realistic conditions. Its 24 classes correspond to 24 letters (A-Y, excluding J) from the American Sign Language (ASL), which we call ASL-DVS. Examples of recordings are shown in Fig 3. The ASL-DVS was recorded with an iniLabs DAVIS240c NVS camera set up in an office environment with low environmental noise and constant illumination. For all recordings, the camera was at the same position and orientation to the persons carrying out the handshapes. Five subjects were asked to pose the different static handshapes relative to the camera in order to introduce natural variance into the dataset. For each letter, we collected 4,200 samples (total of 100,800 samples) and each sample lasts for approximately 100 milliseconds. Fig. 4 shows a comparison of existing NVS datasets w.r.t. the number of classes and total size. Within the landscape of existing datasets, our ASL-DVS is a comparably complex dataset with the largest number of labelled examples. We therefore hope that this will make it a useful resource for researchers to build comprehensive model for NVS-based object recognition, especially given the fact that it comprises real-world recordings. ASL-DVS will be publicly available for download at a link to be provided after the review process is completed. In our experiments, all datasets presented Fig. 4 are used to validate our algorithm.

**Implementation Details:** We discuss implementation details in this section. For simple datasets N-MNIST and MNIST-DVS, our spatial feature learning module is only comprised of two graph residual blocks. Graph residual blocks are described in Section 3.2, and we

Table 1: Top-1 acccuracy of our CNNs w.r.t. the state of the art, other graph convolution networks & deep CNNs.

| Model | N-MNIST | MNIST-DVS | N-Caltech101 | CIFAR10-DVS | N-CARS | ASL-DVS |
|---|---|---|---|---|---|---|
| H-First [57] | 0.712 | 0.595 | 0.054 | 0.077 | 0.561 | - |
| HOTS [39] | 0.808 | 0.803 | 0.210 | 0.271 | 0.624 | - |
| Gabor-SNN [40, 53] | 0.837 | 0.824 | 0.196 | 0.245 | 0.789 | - |
| HATS [75] | **0.991** | 0.984 | 0.642 | 0.524 | 0.902 | - |
| GIN [86] | 0.754 | 0.719 | 0.476 | 0.423 | 0.846 | 0.514 |
| ChebConv [20] | 0.949 | 0.935 | 0.524 | 0.452 | 0.855 | 0.317 |
| GCN [35] | 0.781 | 0.737 | 0.530 | 0.418 | 0.827 | 0.811 |
| MoNet [48] | 0.965 | 0.976 | 0.571 | 0.476 | 0.854 | 0.867 |
| VGG_19 [74] | 0.972 | 0.983 | 0.549 | 0.334 | 0.728 | 0.806 |
| Inception_V4 [78] | 0.973 | 0.985 | 0.578 | 0.379 | 0.864 | 0.832 |
| ResNet_50 [32] | 0.984 | 0.982 | 0.637 | **0.558** | 0.903 | 0.886 |
| G-CNNs | 0.985 | 0.974 | 0.630 | 0.515 | 0.902 | 0.875 |
| RG-CNNs (proposed) | 0.990 | **0.986** | **0.657** | 0.540 | **0.914** | **0.901** |

fix the kernel size $K = 5$ for all convolutional layers outside of the skip connection. We denote a graph convolutional layer as $\mathrm{Conv_g}(c_{\mathrm{in}}, c_{\mathrm{out}})$, fully connected layer as $\mathrm{FC}(c_{\mathrm{in}}, c_{\mathrm{out}})$ and graph residual block as $\mathrm{Res_g}(\mathrm{c_{in}}, \mathrm{c_{out}})$, where $c_{\mathrm{in}}$ and $c_{\mathrm{out}}$ are the input and output channels respectively. Additionally, we denote max graph pooling layers as $\mathrm{MaxP_g}(\mathrm{s_h}, \mathrm{s_w})$, where $s_{\mathrm{h}}$ and $s_{\mathrm{w}}$ represent the cluster size. With this notation, the architecture of our network for these can be written as $\mathrm{Conv_g}(1, 32) \longrightarrow \mathrm{MaxP_g}(2, 2) \longrightarrow \mathrm{Res_g}(32, 64) \longrightarrow \mathrm{MaxP_g}(4, 4) \longrightarrow \mathrm{Res_g}(64, 128) \longrightarrow \mathrm{MaxP_g}(7, 7) \longrightarrow \mathrm{FC}(128, 128) \longrightarrow \mathrm{FC}(128, Q)$, where $Q$ is the number of classes of each dataset. For the remaining datasets, three residual graph blocks are used, and the utilized network architecture is $\mathrm{Conv_g}(1, 64) \longrightarrow \mathrm{MaxP_g}(\mathrm{s_h}, \mathrm{s_w}) \longrightarrow \mathrm{Res_g}(64, 128) \longrightarrow \mathrm{MaxP_g}(\mathrm{s_h}, \mathrm{s_w}) \longrightarrow \mathrm{Res_g}(128, 256) \longrightarrow \mathrm{MaxP_g}(\mathrm{s_h}, \mathrm{s_w}) \longrightarrow \mathrm{Res_g}(256, 512) \longrightarrow \mathrm{MaxP_g}(\mathrm{s_h}, \mathrm{s_w}) \longrightarrow \mathrm{FC}(512, 1024) \longrightarrow \mathrm{FC}(1024, Q)$. Since the datasets are recorded from different sensors, the spatial resolution of each sensor is different (i.e., DAVIS240c: 240×180, DAVIS128 & ATIS: 128×128), leading to various maximum coordinates for the graph. We therefore set the cluster size in pooling layers in two categories; *(i)* N-Caltech101 and ASL-DVS: 4×3, 16×12, 30×23 and 60×45; *(ii)* CIFAR10-DVS and N-CARS: 4×4, 6×6, 20×20 and 32×32. We also compare the proposed residual graph networks (RG-CNNs) with their corresponding plain graph networks (G-CNNs), which utilize the same number of graph convolutional and pooling layers but without the residual connections. The degree of B-spline bases $m$ of all convolutions in this work is set to 1.

For the N-MNIST, MNIST-DVS and N-CARS datasets, we use the predefined training and testing splits, while for N-Caltech101, CIFAR10-DVS and ASL-DVS, we follow the experiment setup of Sironi [75]: 20% of the data is randomly selected for testing and the remaining is used for training. For each sample, events within 30-millisecond length are randomly extracted to input to our object classification framework. During the non-uniform sampling, the maximal number of events $k$ in each space-time volume is set to 8. When constructing graphs, the radius $R$ is 3, weighted parameters $\alpha$ and $\beta$ are set to 1 and $0.5 \times 10^{-5}$, respectively, the maximal connectivity degree $D_{\max}$ for each node is 32, and $T_V = 1/30s$ length events are randomly extracted to form the graph. In order to reduce overfitting, we add dropout with probability 0.5 after the first fully connected layer and also perform data augmentation. In particular, we spatially scale node positions by a randomly sampled factor within $[0.95, 1)$, perform mirroring (randomly flip node positions along 0 and 1 axis with 0.5 probability) and rotate node positions around a specific axis by a randomly sampled factor within $[0, 10]$ in each dimension. Networks are trained with the Adam optimizer and the cross-entropy loss between softmax output and the one-hot label distribution for 150 epochs with batch size 64 and learning rate 0.001 step-wise decreasing by 0.1 after 60 and 110 epochs.

**Results:** We compare Top-1 classification accuracy obtained from our model with that from HOTS [39], H-First [57], SNN [40, 53] and HATS [75]. For SNN, the results are previously published, while for HOTS, H-First and HATS, we report results from Sironi [75], since we use the same training and testing methodology. The results are shown in Table 1. For the simple N-MNIST and MNIST-DVS datasets, whose accuracy is already close to near-perfect classification, our models achieve comparable results. For the other datasets, our proposed RG-CNNs consistently set the new state-of-the-art on these datasets.

Table 1 also includes the classification results stemming from other graph convolutional networks. The architectures of all control networks are the same as our plain graph networks (G-CNNs) introduced in in this section, with the only

Table 2: Complexity (GFLOPs) and size (MB) of networks.

| Model | GFLOPs | Size (MB) |
|---|---|---|
| VGG_19 [74] | 19.63 | 143.65 |
| Inception_V4 [78] | 12.25 | 42.62 |
| ResNet_50 [32] | 3.87 | 25.61 |
| G-CNNs | 0.39 | 18.81 |
| RG-CNNs | 0.79 | 19.46 |

difference being the graph convolutional operation. Here we consider four other graph convolution operations: GCN [35], ChebConv [20], MoNet [48] and GIN [86]. The training details and data augmentation methods are the same as illustrated before. The Top-1 classification accuracy stemming from all networks of Table 1 indicates that our proposed RG-CNN and G-CNN outperform all the other graph convolutional networks.

In order to further validate our proposal, we compare our results with conventional deep convolutional networks. There are no conventional CNNs specifically designed for NVS events, so we train/evaluate on three well-established CNNs, namely VGG_19 [74], Inception_V4 [78] and ResNet_50 [32]. The format of the required input for these CNNs is frame-based, so we group neuromorphic spike events to frame form similar to the grouping images of Zhu [88]. We thereby introduce a two-channel event image form with the same resolution as the NVS sensor: the two channels encode the number of positive and negative events that have occurred at each position. In addition, each frame grouping corresponds to a random time segment of 30 ms of spike events. To avoid the overfitting, we supplement the training with heavy data augmentation: first, we resize the input images such that the smaller side is 256 and keep the aspect ratio, then use a random cropping of 224×224 spatial samples of the resized frame, finally the cropped volume is randomly flipped and normalized according to its mean and standard deviation. We train all CNNs from scratch using stochastic gradient descent with momentum set to 0.9 and $L_2$ regularization set to $0.1 \times 10^{-4}$, and the learning rate is initialized at $10^{-3}$ and decayed by a factor of 0.1 every 10k iterations.

The Top-1 classification accuracy of all networks is reported in Table 1. As to reference networks, despite performing comprehensive data augmentation and $L_2$ regularization to avoid overfitting, the results acquired from conventional CNNs are still below the-state-of-the-art since event images contain far less information (see Fig. 1). However, except for the CIFAR10-DVS dataset, the accuracy of our proposals surpasses that of conventional frame-based deep CNNs.

**Complexity Analysis:** We now turn our attention to the complexity of our proposals and compare the number of floating-point operations (FLOPs) and the number of parameters of each model. In conventional CNNs, we compute FLOPs for convolution layers as [47]:

$$\text{FLOPs} = 2HW(C_{\text{in}}K^2 + 1)C_{\text{out}} \tag{10}$$

where $H$, $W$ and $C_{\text{in}}$ are height, width and the number of channels of the input feature map, $K$ is the kernel size, and $C_{\text{out}}$ is the number of output channels. For graph convolution layers, FLOPs stem from 3 parts [27]; *(i)* for computation of B-spline bases, there are $N_{\text{edge}}(m+1)^d$ threads each performing $7d$ FLOPs (4 additions and 3 multiplications), where $N_{\text{edge}}$ is the number of edges, $m$ the B-spline basis degree and $d$ the dimension of graph coordinates; *(ii)* for convolutional operations, the FLOPs count is $3N_{\text{edge}}C_{\text{in}}C_{\text{out}}(m+1)^d$ , with factor 3 stemming from 1 addition and 2 multiplications in the inner loop of each kernel and $C_{\text{in}}$ and $C_{\text{out}}$ is the number of input and output channels, respectively; *(iii)* for scatter operations and the bias term, the FLOPs count is $(N_{\text{edge}} + N_{\text{node}})C_{\text{out}}$, where $N_{\text{node}}$ is the number of nodes. In total, we have

$$\begin{aligned} \text{FLOPs} &= N_{\text{edge}}(m+1)^d(3C_{\text{in}}C_{\text{out}} + 7d) \\ &+ (N_{\text{edge}} + N_{\text{node}})C_{\text{out}} \end{aligned} \tag{11}$$

For fully connected layers, in both conventional CNNs and GCNs, we compute FLOPs as [47] $\text{FLOPs} = (2I-1)O$, where $I$ is the input dimensionality and $O$ is the output dimensionality. As to the number of parameters, for each convolution layer in both CNNs and GCNs, it is $(C_{\text{in}}K^2 + 1)C_{\text{out}}$, while in fully connected layers, it is $(C_{\text{in}}+1)C_{\text{out}}$. As shown by (11), FLOPs of graph convolution depend on the number of edges and nodes. Since the size of input graph varies per dataset, we opt to report representative results from N-Caltech101 in Table 2. G-CNNS and RG-CNNs have the smaller number of weights and require the less computation compared to deep CNNs. The main reason is that the graph representation is compact, which in turn reduces the amount of data needed to be processed. For N-Caltech101, the average number of nodes of each graph is 1,000, while grouping events to 2-channel image makes the input size equal to 86,400.

### 4.2. Action Recognition

Action recognition has numerous applications in intelligent surveillance, human behavior analysis, and other motion-based tasks. In this section, we first introduce datasets for evaluation, including our new UCF101_DVS and HMDB51_DVS datasets and the associated recording process. We then proceed to discussing implementation details for our action recognition framework, detailing the architectures of the spatial feature learning module, Graph2Grid block and temporal feature learning module. Finally, we present results and complexity analysis on datasets for variants of our framework and other recent state-of-the-art methods.

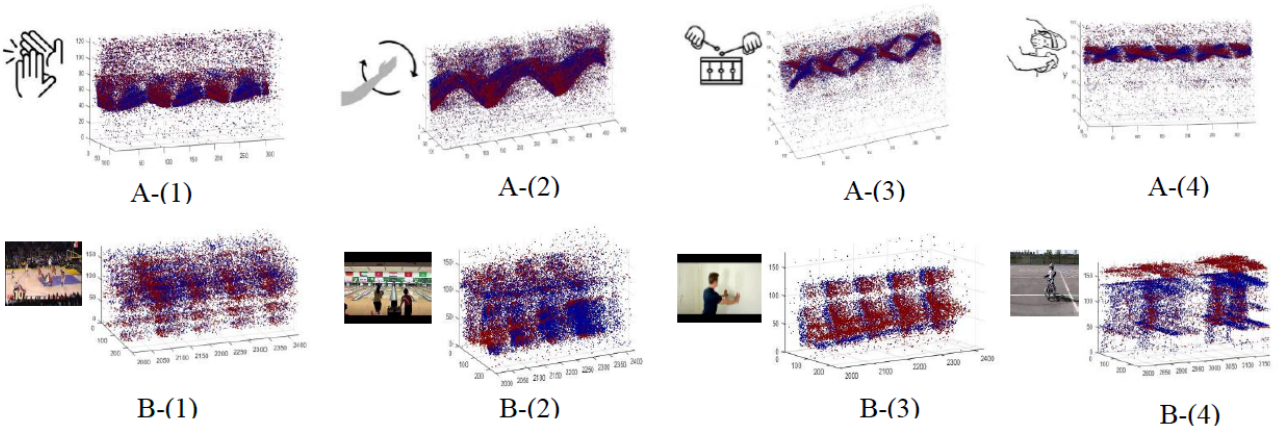


Figure 5: Visualization of samples from DVS128 Gesture Dataset and UCF101_DVS. (A) DVS128 Gesture Dataset: A-1: hand clap; A-2: right hand rotation clockwise; A-3: air drums; A-4: forearm roll. (B) UCF101_DVS: B-1: basketball dunk; B-2: bowling; B-3: wall pushups; B-4: biking

**Datasets:** Most action recognition methods for neuromorphic vision sensing are tested on the DVS128 Gesture Dataset[2] and posture dataset[87]. The DVS128 Gesture Dataset comprises 1,342 instances of a set of 11 hand and arm gestures and posture dataset includes only three human actions; namely, consisting of 191 bend, 175 sit-stand and 118 walk actions. Both of them are collected from experimental setting environment with clean background. These datasets are simple and have limited number in both size and class; as such, they cannot represent complex real-life scenarios and are not robust to evaluation for advanced algorithms. Moreover, while useful for early-stage attempts, algorithms[2, 87, 58, 85] evaluated on these datasets (including our framework) already achieve high accuracy. Therefore, it is necessary to establish larger and more complex datasets for algorithm evaluation in the NVS domain.

In the active pixel sensing (APS) domain, UCF101 [76] and HMDB [37] are widely used to evaluate the performance of the algorithms. UCF-101 has 13,320 videos with 101 different human actions and HMDB-51 has about 7,000 videos with 51 human action categories. We therefore propose to convert these datasets to the neuromorphic domain; this requires recording the APS videos with an NVS camera. Recent work by Hu *et al.* [33] recorded UCF-51, by displaying existing benchmark videos on a monitor and recording with a stationary a neuromorphic vision sensor under controlled lighting conditions; however UCF-51 only represents a small subset of UCF-101 over 51 classes. Conversely, we follow the same recording protocol of [33] and record the *remaining* of UCF-101 and HMDB-51. Each video is displayed by a monitor that is set to its highest brightness and contrast setting. The display is recorded by a neuromorphic vision sensor DAVIS240c that is adjusted to cover the region of interest on the monitor. The recording is set in a dark room where only the monitor is the light source. In this way, we generate the largest neuromorphic datasets available for action recognition, which also correspond with the standard datasets evaluated on in the APS domain. We refer to these NVS datasets as UCF101_DVS and HMDB51_DVS respectively. These datasets will be open public for the community use as one of contribution of these paper.

**Implementation Details:** The number of graphs $S$ constructed from the event stream is set to either 8 or 16; we present results for both settings in the tables below. For each volume, events within 1/30s ($T_V = 1/30$s) are constructed into one spatial graph, and each node in graph is connected to its nearest nodes ($K = 1$). We utilize our proposed residual graph CNNs (RG-CNN) for the spatial feature learning module. For simple datasets such as the DVS128 Gesture Dataset, only two residual blocks are stacked, each followed by a graph max pooling layer. We use the same notation as in 4.1 for parameter illustration and the architecture for this module is $\mathrm{Conv_g}(1,64) \longrightarrow \mathrm{MaxP_g}(2,2) \longrightarrow \mathrm{Res_g}(64,128) \longrightarrow \mathrm{MaxP_g}(4,4)$. Conversely, for more complex datasets, such as UCF101_DVS and HMDB51_DVS, three residual blocks are used and the details is $\mathrm{Conv_g}(1,32) \longrightarrow \mathrm{MaxP_g}(2,2) \longrightarrow \mathrm{Res_g}(32,64) \longrightarrow \mathrm{MaxP_g}(4,3) \longrightarrow \mathrm{Res_g}(64,128) \longrightarrow \mathrm{MaxP_g}(8,6)$. For the temporal feature learning module, we explore three types of architecture as described in Section 3.4:

- *Plain 3D:* For plain 3D CNN, we consider a series of consecutive 3D convolutional and pooling layers, where each intermediate convolution layer is followed by batch normalization layer and a ReLU activation function. We refer to a traditional 3D convolution layer with batch normalization and activation function as $\mathrm{Conv_{3D}}(c_{\mathrm{in}}, c_{\mathrm{out}})$, where $c_{\mathrm{in}}$ and $c_{\mathrm{out}}$ are the number of input and output channels respectively. 3D max pooling and global average pooling are denoted as $\mathrm{MaxP_{3D}}$ and GlobAvgP respectively, fully con-

nected layer as FC and number of task classes as $Q$. The plain 3D convolution architecture can thus be represented as follows (assuming 128 input channels after the Graph2Grid block): $\text{Conv}_{3D}(128, 128) \longrightarrow \text{MaxP}_{3D} \longrightarrow \text{Conv}_{3D}(128, 256) \longrightarrow \text{MaxP}_{3D} \longrightarrow \text{Conv}_{3D}(256, 512) \longrightarrow \text{MaxP}_{3D} \longrightarrow \text{Conv}_{3D}(512, 512) \longrightarrow \text{MaxP}_{3D} \longrightarrow \text{GlobAvgP} \longrightarrow \text{FC}(Q)$. With notation $(h, w, t)$ denoting height, width and time dimensions, we note that the kernel size and stride in every convolution layer is $(3, 3, 3)$ and $(1, 1, 1)$ respectively, and the window size and stride in all 3D max pooling layers is $(2, 2, 2)$, expect for the first pooling layer, where the stride is $(2, 2, 1)$ (to ensure that there is not too aggressive a temporal downscaling early on).

- *Inception-3D(4):* We also consider an Inception-3D based architecture, comprising a series of 4 consecutive ID blocks. In order to ensure that the temporal feature learning does not become a bottleneck in the end-to-end framework, we restrict the number of I3D blocks to four. Our implementation of the I3D block matches that described by Carreira *et al.* [15], as the concatenation of four streams of convolution layers with varying kernel size. With max pooling and global average pooling defined as above, and the $b$-th I3D block denoted in shorthand form as $\text{Inc}_b(c_{in}, c_{out})$, our architecture can represented as follows: $\text{Inc}_1(128, 480) \longrightarrow \text{Pool3D} \longrightarrow \text{Inc}_2(480, 512) \longrightarrow \text{Pool3D} \longrightarrow \text{Inc}_3(512, 512) \longrightarrow \text{Pool3D} \longrightarrow \text{Inc}_4(512, 512) \longrightarrow \text{Pool3D} \longrightarrow \text{AvgPool} \longrightarrow \text{FC}(Q)$. The kernel size and pooling window size and stride is set equivalently to the plain 3D convolution networks above. The number of output channels of the $n$-th convolutional layer for the $s$-th stream is labelled as $c_{out}[s][n]$. We can present with nested lists the number of output channels per convolutional layer for each I3D block:
$\text{Inc}_1$=[[128], [128, 192], [32, 96], 64],
$\text{Inc}_2$=[[192], [96, 208], [16, 48], 64],
$\text{Inc}_3$=[[160], [112, 224], [24, 64], 64],
$\text{Inc}_4$=[[128], [128, 256], [24, 64], 64].
For example, for $\text{Inc}_1$, this corresponds to a single convolutional layer with 128 output channels in the first stream, two convolutional layers with 128 and 192 output channels respectively in the second stream, etc.

- *Residual 3D:* Finally, we consider 3D residual CNNs, where we effectively replace the I3D block with a 3D residual block. The 3D residual block design for temporal feature learning is illustrated in Fig. 2; essentially, there are two 3D convolutional layers in the base stream of the block, with a non-linear residual connection from the input of the first to the output of the second layer. We can define a 3D residual block as $\text{Res}(c_{in}, c_{inter}, c_{out})$, where $c_{inter}$ represents the number of input channels to the second convolutional layer in the base stream and $c_{in}$ and $c_{out}$ are the number of input and output channels respectively to the residual block. The 3D residual CNN is defined as follows: $\text{Res}(128, 256, 512) \longrightarrow \text{Pool3D} \longrightarrow \text{Res}(512, 512, 1024) \longrightarrow \text{Pool3D} \longrightarrow \text{GlobAvgP} \longrightarrow \text{FC}(Q)$. Again, denoting $(h, w, t)$ as the height, width and time dimensions, the kernel size is (3,3,3) and stride is (1,1,1) for all convolutional layers in the base stream, and all 3D max_pooling layers are as defined for the plain 3D CNN.

Sampled graphs are spatially scaled by a randomly sampled factor within $(0.8, 1)$ and randomly left-right flipped with probability $0.5$. We use the predefined training and test set for DVS128 Gesture Dataset and for UCF101_DVS and HMDB51_DVS, we use the training/test splits (standard Split1) defined for their APS counterparts (UCF-101 and HMDB-51). Networks are trained with the Adam optimizer and the cross-entropy loss between softmax output and the one-hot label distribution for 150 epochs with batch size 32 and 16 for $S = 8$ and $S = 16$ respectively. The learning rate is set to 0.001, with stepwise decay by a factor of 0.1 after 60 and 100 epochs.

**Reference Networks:** We compare action recognition results of our proposed RG-CNN + Plain 3D, RG-CNN + Incep. 3D(4) and RG-CNN + Res. 3D with reference networks from the APS video domain repurposed for the NVS domain. Here, we include C3D [80], I3D [15], 3D ResNet with 34 layers [32], P3D with 63 layers [66], R2+1D [81] and 3D ResNext with 50 layers [31]. In contrast to our framework, these networks are entirely grid-based and require artificial grouping of events into frame form. Therefore, to feed these networks we follow a similar approach to Chadha *et al.* [16], and construct a single frame by summing events within a 1/30s duration at each spatial position of the NVS sensor. The resulting event frame has two channels, as ON and OFF events are grouped independently. We generate $S = 8$ or $S = 16$ frames from event volumes, in order to align with the number of input graphs utilized in our framework. To avoid over-fitting during training, we supplement the training with data augmentation: first, we normalize the input and re-size the input frames such that the smaller side is 128 (178 for P3D, 256 for I3D) and keep the aspect ratio, then use a random cropping of $112 \times 112$ ($160 \times 160$ for P3D, $224 \times 224$ for I3D) spatial samples of the re-sized frame, finally the cropped volume is randomly left-right flipped. We train all models from scratch using

stochastic gradient descent with momentum set to 0.9, and the learning rate is initialized at 0.01 and decayed by a factor of 0.1 every 50 epochs.

**Results:** We first evaluate our method on the DVS128 Gesture Dataset, and compare with both recent state-of-the-art methods and reference networks. The results are shown in Table 3. In these recent methods, the event recording duration considered is 0.25 and 0.5 seconds, we follow the same set up to set the number of graphs, enabling a fair comparison. Examining the results, we see that the LSTM-based method [69] is outperformed by other methods. We attribute this to the fact that the LSTM method regards event streams as pure temporal sequences and only learns the temporal features from the events, without encoding spatial dependencies. On the contrary, PointNet-based methods [64, 65, 85] take the input as a point cloud and learn to summarize the geometric features, which boosts accuracy. With regards to reference networks, although I3D[15] and 3D ResNet_34 [32] perform spatio-temporal feature learning, there is no explicit modelling of event dependencies as events are directly grouped into frames. As such, our proposal outperforms all existing works and reference networks on this dataset and sets a new benchmark. We attribute this to the combination of our graph representation, spatial feature learning and temporal feature learning over multiple graphs, which results in learning a more informative spatio-temporal representation of the input.

Table 3: Top-1 classification accuracy of DVS128 Gesture Dataset.

| Model | Duration (0.25s) | Duration (0.5s) |
|---|---|---|
| LSTM [69] | 0.882 | 0.865 |
| PointNet [64] | 0.887 | 0.902 |
| PointNet++ [65] | 0.923 | 0.941 |
| Amir CVPR2017 [2] | - | 0.945 |
| Wang WACV2019 [85] | 0.940 | 0.953 |
| ResNet_34 [32] | 0.943 | 0.955 |
| I3D [15] | 0.951 | 0.965 |
| RG-CNN + Plain 3D | 0.954 | 0.968 |
| RG-CNN + Incep. 3D(4) | 0.957 | 0.968 |
| RG-CNN + Res. 3D | **0.961** | **0.972** |

As shown in Fig. 5, DVS128 Gesture Dataset is too simple since we can see evident pattern difference, while UCF101_DVS is complex events volumes. And also, as shown in Table 3, the results on DVS128 Gesture Dataset are already close to perfect accuracy. Therefore, we further evaluate our algorithms on our newly introduced datasets, UCF101_DVS and HMDB51_DVS, which contains more classes and overall present a more challenging task for action recognition. We note that when evaluating current NVS-based methods for action recognition on UCF101_DVS and HMDB51_DVS, the accuracy obtainable is only around 5%-7%, since these methods only perform spatial (PointNet, PointNet++) or temporal (LSTM) feature learning, and thus learn degenerate solutions. Therefore, we focus our comparison on reference networks for these datasets.

The Top-1 recognition accuracy of all networks is reported in Table 4 for UCF101_DVS and HMDB51_DVS. We again present results on our framework for Plain 3D, Inecption-3D(4) and Residual 3D variants of our temporal feature learning module and compare directly with reference networks. As is evident, the reference networks are outperformed by our variants of our model. Specifically, the highest performance obtained from reference models is from I3D, while our base model (RG-CNN + Plain 3D) outperforms I3D by 3.3% and 6.1% in terms of UCF101_DVS and HMDB51_DVS when $S = 8$ inputs constructed from the event stream, respectively. Note that when varying the temporal feature learning architecture from Plain 3D, to Inception-3D(4) and Residual 3D, our model performance increases slightly, due to the higher capacity of these architectures.

**Complexity Analysis:** We compare the complexity of our proposed spatio-temporal feature learning framework with reference networks, with respect to the number of floating-point operations (FLOPs) and the number of parameters. FLOPs and parameter computation of graph convolution and fully connected networks are the same as described in Section 4.2. For conventional 3D convolution we compute FLOPs as

$$\text{FLOPs} = 2HWT(C_{\text{in}}K^3 + 1)C_{\text{out}} \tag{12}$$

where $H$, $W$, $T$ and $C_{\text{in}}$ are height, width, temporal length and the number of channels of the input feature map, $K$ is the kernel size, and $C_{\text{out}}$ is the number of output channels. As to the number of parameters of 3D convolution, it is $(C_{\text{in}}K^3 + 1)C_{\text{out}}$. As described in Section 4.2, the FLOPs of graph convolution depend on the number of edges and nodes. Since the size of input graph varies per dataset, we opt to report representative results from UCF101_DVS in Table 5. For each sample, 16 graphs are sampled as inputs to spatial feature learning module, and the FLOPs in this module is the average of whole UCF_DVS dataset. As to CNN-based networks, the input size $(C, T, H, W)$ (where $C$, $T$, $H$, $W$ are the number of channels, temporal size, height and width of frame, respectively) for I3D is $(2, 16, 224, 224)$, for P3D_63 is $(2, 16, 160, 160)$, while for others are $(2, 16, 112, 112)$. The results shows that our model provide a smaller size compared to all reference networks. As to computation complexity, though the our models need more computation than P3D_63 and ResNext_50, they achieve better performance in all three applications.

Table 4: Top-1 classification accuracy of UCF101_DVS and HMDB51_DVS w.r.t. various model.

| Model | UCF101_DVS | | HMDB51_DVS | |
|---|---|---|---|---|
| | $S = 8$ | $S = 16$ | $S = 8$ | $S = 16$ |
| C3D [80] | 0.382 | 0.472 | 0.342 | 0.417 |
| ResNet_34 [32] | 0.513 | 0.579 | 0.350 | 0.438 |
| P3D_63 [66] | 0.484 | 0.534 | 0.343 | 0.404 |
| R2+1D_36 [81] | 0.496 | 0.628 | 0.312 | 0.419 |
| ResNext_50 [31] | 0.515 | 0.602 | 0.317 | 0.394 |
| I3D [15] | 0.596 | 0.635 | 0.386 | 0.466 |
| RG-CNN + Plain D | 0.629 | 0.663 | 0.447 | 0.494 |
| RG-CNN + Incep. 3D(4) | **0.632** | **0.678** | 0.452 | **0.515** |
| RG-CNN + Res. 3D | 0.627 | 0.673 | **0.455** | 0.497 |

Performance acquired by I3D is close to that from our models, while its computation complexity is double or almost triple.

Table 5: Comparison of networks w.r.t. complexity (GFLOPs) and size (MB) of networks.

| Model | FLOPs ($\times 10^9$) | #params ($\times 10^6$) |
|---|---|---|
| C3D [80] | 39.69 | 78.41 |
| ResNet_34 [32] | 11.64 | 63.70 |
| P3D_63 [66] | 8.30 | 25.74 |
| R2+1D_36 [81] | 41.77 | 33.22 |
| ResNext_50 [31] | 6.46 | 26.05 |
| I3D [15] | 30.11 | 12.37 |
| RG-CNN + Plain 3D | 12.46 | 6.95 |
| RG-CNN + Incep. 3D(4) | 12.39 | 3.86 |
| RG-CNN + Res. 3D | 13.72 | 12.43 |

## 5. Conclusion

In this work we develop an end-to-end trainable and graph-based feature learning framework for neuromorphic vision sensing. We first represent neuromorphic events as graphs, which are explicitly aligned with the compact and non-uniform sampling of NVS hardware. We couple this with an efficient end-to-end learning framework, comprising graph convolutional networks for spatial feature learning directly from graph inputs. We extend our framework with our Graph2Grid module that converts the graphs to grid representations for coarse temporal feature learning with conventional 3D CNNs. We demonstrate how this framework can be employed for both object classification and action recognition and evaluate our framework on both tasks with standard datasets. We additionally propose and make available three large-scale neuromorphic dataset in order to motivate further progress in the field. Finally, our results on all datasets show that we outperform all recent NVS based proposals while maintaining lower complexity.

## References


[1] F. Akopyan, J. Sawada, A. Cassidy, R. Alvarez-Icaza, J. Arthur, P. Merolla, N. Imam, Y. Nakamura, P. Datta, G.-J. Nam, et al. Truenorth: Design and tool flow of a 65 mw 1 million neuron programmable neurosynaptic chip. *IEEE Transactions on Computer-Aided Design of Integrated Circuits and Systems*, 34(10):1537–1557, 2015. 4

[2] A. Amir, B. Taba, D. Berg, T. Melano, J. McKinstry, C. Di Nolfo, et al. A low power, fully event-based gesture recognition system. In *Proceedings of the IEEE Conference on Computer Vision and Pattern Recognition*, pages 7243–7252, 2017. 2, 3, 4, 11, 13

[3] F. Barranco, C. Fermüller, and Y. Aloimonos. Contour motion estimation for asynchronous event-driven cameras. *Proceedings of the IEEE*, 102(10):1537–1556, 2014. 3

[4] F. Barranco, C. Fermuller, and Y. Aloimonos. Bio-inspired motion estimation with event-driven sensors. In *International Work-Conference on Artificial Neural Networks*, pages 309–321. Springer, 2015. 3

[5] R. Benosman, C. Clercq, X. Lagorce, S.-H. Ieng, and C. Bartolozzi. Event-based visual flow. *IEEE transactions on neural networks and learning systems*, 25(2):407–417, 2014. 3

[6] R. Berner, T. Delbruck, A. Civit-Balcells, and A. Linares-Barranco. A 5 meps 100 usb2. 0 address-event monitor-sequencer interface. In *2007 IEEE International Symposium on Circuits and Systems*, pages 2451–2454. IEEE, 2007. 1

[7] Y. Bi and Y. Andreopoulos. Pix2nvs: Parameterized conversion of pixel-domain video frames to neuromorphic vision streams. In *2017 IEEE International Conference on Image Processing (ICIP)*, pages 1990–1994. IEEE, 2017. 8

[8] O. Bichler, D. Querlioz, S. J. Thorpe, J.-P. Bourgoin, and C. Gamrat. Extraction of temporally correlated features from dynamic vision sensors with spike-timing-dependent plasticity. *Neural Networks*, 32:339–348, 2012. 2, 4

[9] D. Boscaini, J. Masci, E. Rodolà, and M. Bronstein. Learning shape correspondence with anisotropic convolutional neural networks. In *Advances in Neural Information Processing Systems*, pages 3189–3197, 2016. 5, 6

[10] M. M. Bronstein, J. Bruna, Y. LeCun, A. Szlam, and P. Vandergheynst. Geometric deep learning: going beyond euclidean data. *IEEE Signal Processing Magazine*, 34(4):18–42, 2017. 5

[11] T. Brosch, S. Tschechne, and H. Neumann. On event-based optical flow detection. *Frontiers in neuroscience*, 9:137, 2015. 3

[12] J. Bruna, W. Zaremba, A. Szlam, and Y. LeCun. Spectral networks and locally connected networks on graphs. *arXiv preprint arXiv:1312.6203*, 2013. 5

[13] M. Cannici, M. Ciccone, A. Romanoni, and M. Matteucci. Attention mechanisms for object recognition with event-based cameras. *arXiv preprint arXiv:1807.09480*, 2018. 2, 3

[14] M. Cannici, M. Ciccone, A. Romanoni, and M. Matteucci. Event-based convolutional networks for object detection in neuromorphic cameras. *arXiv preprint arXiv:1805.07931*, 2018. 2, 3

[15] J. Carreira and A. Zisserman. Quo vadis, action recognition? a new model and the kinetics dataset. In *proceedings of the IEEE Conference on Computer Vision and Pattern Recognition*, pages 6299–6308, 2017. 1, 7, 12, 13, 14

[16] A. Chadha, Y. Bi, A. Abbas, and Y. Andreopoulos. Neuromorphic vision sensing for cnn-based action recognition. In *ICASSP 2019-2019 IEEE International Conference on Acoustics, Speech and Signal Processing (ICASSP)*, pages 7968–7972. IEEE, 2019. 3, 12

[17] X. Clady, S.-H. Ieng, and R. Benosman. Asynchronous event-based corner detection and matching. *Neural Networks*, 66:91–106, 2015. 3

[18] X. Clady, J.-M. Maro, S. Barré, and R. B. Benosman. A motion-based feature for event-based pattern recognition. *Frontiers in neuroscience*, 10:594, 2017. 2, 3

[19] G. K. Cohen. *Event-based feature detection, recognition and classification*. PhD thesis, Paris 6, 2016. 2, 3

[20] M. Defferrard, X. Bresson, and P. Vandergheynst. Convolutional neural networks on graphs with fast localized spectral filtering. In *Advances in neural information processing systems*, pages 3844–3852, 2016. 5, 9, 10

[21] T. Delbruck. Neuromorphic vision sensing and processing. In *Europ. Solid-State Dev. Res. Conf*, pages 7–14, 2016. 1, 2

[22] T. Delbrück, B. Linares-Barranco, E. Culurciello, and C. Posch. Activity-driven, event-based vision sensors. In *Proceedings of 2010 IEEE International Symposium on Circuits and Systems*, pages 2426–2429. IEEE, 2010. 1

[23] J. Deng, W. Dong, R. Socher, L.-J. Li, K. Li, and L. Fei-Fei. Imagenet: A large-scale hierarchical image database. In *2009 IEEE conference on computer vision and pattern recognition*, pages 248–255. Ieee, 2009. 1

[24] P. U. Diehl and M. Cook. Unsupervised learning of digit recognition using spike-timing-dependent plasticity. *Frontiers in computational neuroscience*, 9:99, 2015. 2, 4

[25] P. U. Diehl, D. Neil, J. Binas, M. Cook, S.-C. Liu, and M. Pfeiffer. Fast-classifying, high-accuracy spiking deep networks through weight and threshold balancing. In *2015 International Joint Conference on Neural Networks (IJCNN)*, pages 1–8. IEEE, 2015. 4

[26] C. Feichtenhofer, A. Pinz, and A. Zisserman. Convolutional two-stream network fusion for video action recognition. In *Proceedings of the IEEE conference on computer vision and pattern recognition*, pages 1933–1941, 2016. 2, 5

[27] M. Fey, J. Eric Lenssen, F. Weichert, and H. Müller. Splinecnn: Fast geometric deep learning with continuous b-spline kernels. In *Proceedings of the IEEE Conference on Computer Vision and Pattern Recognition*, pages 869–877, 2018. 5, 6, 10

[28] G. P. García, P. Camilleri, Q. Liu, and S. Furber. pydvs: An extensible, real-time dynamic vision sensor emulator using off-the-shelf hardware. In *2016 IEEE Symposium Series on Computational Intelligence (SSCI)*, pages 1–7. IEEE, 2016. 8

[29] R. Ghosh, A. Gupta, A. Nakagawa, A. Soares, and N. Thakor. Spatiotemporal filtering for event-based action recognition. *arXiv preprint arXiv:1903.07067*, 2019. 2, 3

[30] R. Girshick. Fast r-cnn. In *Proceedings of the IEEE international conference on computer vision*, pages 1440–1448, 2015. 1

[31] K. Hara, H. Kataoka, and Y. Satoh. Can spatiotemporal 3d cnns retrace the history of 2d cnns and imagenet? In *Proceedings of the IEEE conference on Computer Vision and Pattern Recognition*, pages 6546–6555, 2018. 12, 14

[32] K. He, X. Zhang, S. Ren, and J. Sun. Deep residual learning for image recognition. In *Proceedings of the IEEE conference on computer vision and pattern recognition*, pages 770–778, 2016. 6, 9, 10, 12, 13, 14

[33] Y. Hu, H. Liu, M. Pfeiffer, and T. Delbruck. Dvs benchmark datasets for object tracking, action recognition, and object recognition. *Frontiers in neuroscience*, 10:405, 2016. 11

[34] S. Ioffe and C. Szegedy. Batch normalization: Accelerating deep network training by reducing internal covariate shift. *ICML*, 2015. 6

[35] T. N. Kipf and M. Welling. Semi-supervised classification with graph convolutional networks. *ICLR*, 2017. 9, 10

[36] A. Krizhevsky, I. Sutskever, and G. E. Hinton. Imagenet classification with deep convolutional neural networks. In *Advances in neural information processing systems*, pages 1097–1105, 2012. 1

[37] H. Kuehne, H. Jhuang, E. Garrote, T. Poggio, and T. Serre. Hmdb: a large video database for human motion recognition. In *2011 International Conference on Computer Vision*, pages 2556–2563. IEEE, 2011. 11

[38] X. Lagorce, G. Orchard, F. Galluppi, B. E. Shi, and R. B. Benosman. Hots: a hierarchy of event-based time-surfaces for pattern recognition. *IEEE transactions on pattern analysis and machine intelligence*, 39(7):1346–1359, 2016. 3

[39] X. Lagorce, G. Orchard, F. Galluppi, B. E. Shi, and R. B. Benosman. Hots: a hierarchy of event-based time-surfaces for pattern recognition. *IEEE transactions on pattern analysis and machine intelligence*, 39(7):1346–1359, 2017. 2, 9

[40] J. H. Lee, T. Delbruck, and M. Pfeiffer. Training deep spiking neural networks using backpropagation. *Frontiers in neuroscience*, 10:508, 2016. 4, 9

[41] K. Lee, H. Woo, and T. Suk. Point data reduction using 3d grids. *The International Journal of Advanced Manufacturing Technology*, 18(3):201–210, 2001. 5

[42] H. Li, H. Liu, X. Ji, G. Li, and L. Shi. Cifar10-dvs: an event-stream dataset for object classification. *Frontiers in neuroscience*, 11:309, 2017. 8

[43] Q. Li, Z. Han, and X.-M. Wu. Deeper insights into graph convolutional networks for semi-supervised learning. In *Thirty-Second AAAI Conference on Artificial Intelligence*, 2018. 6

[44] P. Lichtsteiner, C. Posch, and T. Delbruck. A 128x128, 120 db 30mw latency asynchronous temporal contrast vision sensor. *IEEE journal of solid-state circuits*, 43(2):566–576, 2008. 8

[45] W. Liu, D. Anguelov, D. Erhan, C. Szegedy, S. Reed, C.-Y. Fu, and A. C. Berg. Ssd: Single shot multibox detector. In *European conference on computer vision*, pages 21–37. Springer, 2016. 1

[46] J. Masci, D. Boscaini, M. Bronstein, and P. Vandergheynst. Geodesic convolutional neural networks on riemannian manifolds. In *Proceedings of the IEEE international conference on computer vision workshops*, pages 37–45, 2015. 5, 6

[47] P. Molchanov, S. Tyree, T. Karras, T. Aila, and J. Kautz. Pruning convolutional neural networks for resource efficient inference. *ICLR*, 2017. 10

[48] F. Monti, D. Boscaini, J. Masci, E. Rodola, J. Svoboda, and M. M. Bronstein. Geometric deep learning on graphs and manifolds using mixture model cnns. In *Proceedings of the IEEE Conference on Computer Vision and Pattern Recognition*, pages 5115–5124, 2017. 5, 6, 9, 10

[49] E. Mueggler, C. Bartolozzi, and D. Scaramuzza. Fast event-based corner detection. In *British Machine Vis. Conf.(BMVC)*, volume 1, 2017. 3

[50] E. Mueggler, H. Rebecq, G. Gallego, T. Delbruck, and D. Scaramuzza. The event-camera dataset and simulator: Event-based data for pose estimation, visual odometry, and slam. *The International Journal of Robotics Research*, 36(2):142–149, 2017. 3, 8

[51] E. Neftci, S. Das, B. Pedroni, K. Kreutz-Delgado, and G. Cauwenberghs. Event-driven contrastive divergence for spiking neuromorphic systems. *Frontiers in neuroscience*, 7:272, 2014. 4

[52] E. Neftci, C. Posch, E. Chicca, and H. Ishibuchi. Neuromorphic engineering. *Computational Intelligence*, 2:278, 2015. 2

[53] D. Neil, M. Pfeiffer, and S.-C. Liu. Phased lstm: Accelerating recurrent network training for long or event-based sequences. In *Advances in Neural Information Processing Systems*, pages 3882–3890, 2016. 9

[54] P. O'Connor, D. Neil, S.-C. Liu, T. Delbruck, and M. Pfeiffer. Real-time classification and sensor fusion with a spiking deep belief network. *Frontiers in neuroscience*, 7:178, 2013. 4

[55] G. Orchard and R. Etienne-Cummings. Bioinspired visual motion estimation. *Proceedings of the IEEE*, 102(10):1520–1536, 2014. 3

[56] G. Orchard, A. Jayawant, G. K. Cohen, and N. Thakor. Converting static image datasets to spiking neuromorphic datasets using saccades. *Frontiers in neuroscience*, 9:437, 2015. 8

[57] G. Orchard, C. Meyer, R. Etienne-Cummings, C. Posch, N. Thakor, and R. Benosman. Hfirst: a temporal approach to object recognition. *IEEE transactions on pattern analysis and machine intelligence*, 37(10):2028–2040, 2015. 3, 9

[58] X. Peng, B. Zhao, R. Yan, H. Tang, and Z. Yi. Bag of events: an efficient probability-based feature extraction method for aer image sensors. *IEEE transactions on neural networks and learning systems*, 28(4):791–803, 2016. 4, 11

[59] X. Peng, B. Zhao, R. Yan, H. Tang, and Z. Yi. Bag of events: an efficient probability-based feature extraction method for aer image sensors. *IEEE transactions on neural networks and learning systems*, 28(4):791–803, 2017. 3

[60] J. A. Pérez-Carrasco, B. Zhao, C. Serrano, B. Acha, T. Serrano-Gotarredona, S. Chen, and B. Linares-Barranco. Mapping from frame-driven to frame-free event-driven vision systems by low-rate rate coding and coincidence processing–application to feedforward convnets. *IEEE transactions on pattern analysis and machine intelligence*, 35(11):2706–2719, 2013. 4

[61] L. Piegl and W. Tiller. *The NURBS book*. Springer Science & Business Media, 2012. 6

[62] C. Posch, D. Matolin, and R. Wohlgenannt. A qvga 143 db dynamic range frame-free pwm image sensor with lossless pixel-level video compression and time-domain cds. *IEEE Journal of Solid-State Circuits*, 46(1):259–275, 2010. 1

[63] C. Posch, D. Matolin, and R. Wohlgenannt. A qvga 143 db dynamic range frame-free pwm image sensor with lossless pixel-level video compression and time-domain cds. *IEEE Journal of Solid-State Circuits*, 46(1):259–275, 2011. 8

[64] C. R. Qi, H. Su, K. Mo, and L. J. Guibas. Pointnet: Deep learning on point sets for 3d classification and segmentation. In *Proceedings of the IEEE Conference on Computer Vision and Pattern Recognition*, pages 652–660, 2017. 4, 13

[65] C. R. Qi, L. Yi, H. Su, and L. J. Guibas. Pointnet++: Deep hierarchical feature learning on point sets in a metric space. In *Advances in neural information processing systems*, pages 5099–5108, 2017. 13

[66] Z. Qiu, T. Yao, and T. Mei. Learning spatio-temporal representation with pseudo-3d residual networks. In *proceedings of the IEEE International Conference on Computer Vision*, pages 5533–5541, 2017. 12, 14

[67] B. Ramesh, H. Yang, G. M. Orchard, N. A. Le Thi, S. Zhang, and C. Xiang. Dart: distribution aware retinal transform for event-based cameras. *IEEE transactions on pattern analysis and machine intelligence*, 2019. 3

[68] S. Ren, K. He, R. Girshick, and J. Sun. Faster r-cnn: Towards real-time object detection with region proposal networks. In *Advances in neural information processing systems*, pages 91–99, 2015. 1

[69] T. N. Sainath, O. Vinyals, A. Senior, and H. Sak. Convolutional, long short-term memory, fully connected deep neural networks. In *2015 IEEE International Conference on Acoustics, Speech and Signal Processing (ICASSP)*, pages 4580–4584. IEEE, 2015. 13

[70] A. Sandryhaila and J. M. Moura. Discrete signal processing on graphs. *IEEE transactions on signal processing*, 61(7):1644–1656, 2013. 5

[71] T. Serrano-Gotarredona and B. Linares-Barranco. Poker-dvs and mnist-dvs. their history, how they were made, and other details. *Frontiers in neuroscience*, 9:481, 2015. 8

[72] D. I. Shuman, S. K. Narang, P. Frossard, A. Ortega, and P. Vandergheynst. The emerging field of signal processing on graphs: Extending high-dimensional data analysis to networks and other irregular domains. *arXiv preprint arXiv:1211.0053*, 2012. 5

[73] K. Simonyan and A. Zisserman. Two-stream convolutional networks for action recognition in videos. In *Advances in neural information processing systems*, pages 568–576, 2014. 1

[74] K. Simonyan and A. Zisserman. Very deep convolutional networks for large-scale image recognition. *arXiv preprint arXiv:1409.1556*, 2014. 9, 10

[75] A. Sironi, M. Brambilla, N. Bourdis, X. Lagorce, and R. Benosman. Hats: histograms of averaged time surfaces for robust event-based object classification. In *Proceedings of the IEEE Conference on Computer Vision and Pattern Recognition*, pages 1731–1740, 2018. 2, 3, 8, 9

[76] K. Soomro, A. R. Zamir, and M. Shah. Ucf101: A dataset of 101 human actions classes from videos in the wild. *arXiv preprint arXiv:1212.0402*, 2012. 11

[77] E. Stromatias, D. Neil, F. Galluppi, M. Pfeiffer, S.-C. Liu, and S. Furber. Scalable energy-efficient, low-latency implementations of trained spiking deep belief networks on spinnaker. In *2015 International Joint Conference on Neural Networks (IJCNN)*, pages 1–8. IEEE, 2015. 4

[78] C. Szegedy, S. Ioffe, V. Vanhoucke, and A. A. Alemi. Inception-v4, inception-resnet and the impact of residual connections on learning. In *Thirty-First AAAI Conference on Artificial Intelligence*, 2017. 9, 10

[79] C. Tan, S. Lallee, and G. Orchard. Benchmarking neuromorphic vision: lessons learnt from computer vision. *Frontiers in neuroscience*, 9:374, 2015. 2

[80] D. Tran, L. Bourdev, R. Fergus, L. Torresani, and M. Paluri. Learning spatiotemporal features with 3d convolutional networks. In *Proceedings of the IEEE international conference on computer vision*, pages 4489–4497, 2015. 1, 7, 12, 14

[81] D. Tran, H. Wang, L. Torresani, J. Ray, Y. LeCun, and M. Paluri. A closer look at spatiotemporal convolutions for action recognition. In *Proceedings of the IEEE conference on Computer Vision and Pattern Recognition*, pages 6450–6459, 2018. 12, 14

[82] V. Vasco, A. Glover, and C. Bartolozzi. Fast event-based harris corner detection exploiting the advantages of event-driven cameras. In *2016 IEEE/RSJ International Conference on Intelligent Robots and Systems (IROS)*, pages 4144–4149. IEEE, 2016. 3

[83] C. Wang, B. Samari, and K. Siddiqi. Local spectral graph convolution for point set feature learning. In *Proceedings of the European Conference on Computer Vision (ECCV)*, pages 52–66, 2018. 5

[84] H. Wang and C. Schmid. Action recognition with improved trajectories. In *Proceedings of the IEEE international conference on computer vision*, pages 3551–3558, 2013. 1

[85] Q. Wang, Y. Zhang, J. Yuan, and Y. Lu. Space-time event clouds for gesture recognition: From rgb cameras to event cameras. In *2019 IEEE Winter Conference on Applications of Computer Vision (WACV)*, pages 1826–1835. IEEE, 2019. 4, 11, 13

[86] K. Xu, W. Hu, J. Leskovec, and S. Jegelka. How powerful are graph neural networks? *ICLR*, 2019. 9, 10

[87] B. Zhao, R. Ding, S. Chen, B. Linares-Barranco, and H. Tang. Feedforward categorization on aer motion events using cortex-like features in a spiking neural network. *IEEE transactions on neural networks and learning systems*, 26(9):1963–1978, 2014. 4, 11

[88] A. Z. Zhu, L. Yuan, K. Chaney, and K. Daniilidis. Ev-flownet: self-supervised optical flow estimation for event-based cameras. *arXiv preprint arXiv:1802.06898*, 2018. 2, 3, 10